

Transition of Defect Patterns from 2D to 3D in Liquid Crystals

Yang Qu, Ying Wei and Pingwen Zhang*

School of Mathematical Sciences, Peking University, Beijing 100871, P.R. China.

Received 2 March 2016; Accepted (in revised version) 5 September 2016

Abstract. Defects arise when nematic liquid crystals are under topological constraints at the boundary. Recently the study of defects has drawn a lot of attention because of the growing theoretical and practical significance. In this paper, we investigate the relationship between two-dimensional defects and three-dimensional defects within nematic liquid crystals confined in a shell. A highly accurate spectral method is used to solve the Landau-de Gennes model to get the detailed static structures of defects. Interestingly, the solution is radial-invariant when the thickness of the shell is sufficiently small. As the shell thickness increases, the solution undergoes symmetry break to reconfigure the disclination lines. We study this three-dimensional reconfiguration of disclination lines in detail under different boundary conditions. In particular, we find that the temperature plays an important role in deciding whether the transition between two-dimensional defects and three-dimensional defects is continuous or discontinuous for the shell with planar anchoring condition on both inner and outer surfaces. We also discuss the characterization of defects in two- and three-dimensional spaces within the tensor model.

PACS: 61.30.Jf, 64.70.mf

Key words: Transition of defects, liquid crystal, Landau-de Gennes model, spectral method.

1 Introduction

Nematic liquid crystals (LCs) are composed of rigid rod-like molecules which tend to parallel align with each other due to inter-molecular interaction. When the alignment of LC molecules is under topological constraints at the boundary, discontinuity in the alignment direction of LCs can form, which is known as defect. Typically, there are point defects and disclination lines [18]. The prediction of defect patterns is of great theoretical and practical interests, and remains to be a difficult problem. Because defect patterns are

*Corresponding author. *Email addresses:* quyang@pku.edu.cn (Y. Qu), wyheyhey@163.com (Y. Wei), pzhang@pku.edu.cn (P. Zhang)

not only affected by the temperature and the constraints, but also affected by the shape of the geometric regions bounding them.

In the past decade, many systematic work has been done on nematic LCs confined on the spherical droplets and the regions outside solid balls. Mkaddem and Gartland [16] investigated the defect patterns of nematic LCs confined in spherical droplet under radial anchoring condition. They obtained the radial hedgehog, ring disclination and split-core solutions by assuming rotational symmetry around the z -axis. Hu et al. [1] obtained three configurations (single-core, double-core and split-core) in the spherical droplet under planar anchoring condition. When spherical colloids are dispersed in nematic LCs with radial anchoring condition on the surface, two configurations (Saturn-ring and dipole) are obtained in the article of Ravnik and Zumer [11]. After enforcing planar anchoring condition on the surface, three stable configurations of boojum cores (single-core, double-core and split-core) are obtained [7].

In this paper, we investigate the defect patterns of nematic LCs confined in spherical shells, which is a recent interesting topic of researches. Such as Vitelli et al. [30] experimentally investigated the defect structures of nematic LCs shells; [10] studied the defect texture of nematic LCs shells by a vector model; [28] and [29] exploited the experiments and computer simulations simultaneously to study the defect in nematic LCs shells; Bates et al. [14] utilized the Monte Carlo simulation to study the nematic ordering confined in shells; and Seyednejad et al. [27] used a finite element method to minimize the free energy functional of nematic LCs shells. Although many experiments and simulation methods were designed to investigate the defect patterns in nematic shells, but they didn't give the local structure of the defect patterns clearly. Due to the complexities of the defect patterns, we need high-fidelity simulations with advanced numerical methods for the nematic LCs shells. In this article, we use the spectral method based on Zernike polynomial expansion [23] and BFGS algorithm [24] to solve the Landau-de Gennes model of nematic LCs shells. By these methods, the relationships between defect patterns and the thickness of the shell, the temperature, and the boundary conditions are investigated systematically. We show that when the shell thickness is small, the defect patterns tend to be radial-invariant, which means that the configuration of every layer is same up to a scaling constant in the shell. We call this kind of structures as two-dimensional (2D) structure. When the shell becomes thicker, defects may undergo dramatic reconfigurations and do not hold the radial-invariant property. We call these defect patterns as three-dimensional (3D) structure. The reconfiguration of the defect patterns between 2D and 3D structures is the emphasis of our study.

It is generally known that defects can be classified by their topological invariants. Lavrentovich [4] elaborated the topological charge by homotopy group theory, which is also called winding number in 2D space [6]. In the case of 2D space, winding number is an appropriate metric, and easy to be understood. But in the case of 3D space, winding number and topological charge are different. We use the winding number on the normal plane of defect points to measure the disclination line in this paper, and discuss the distinctions between the winding number and the topological charge of disclination

lines in Section 3.2. The rest of this paper is organized as follows. In Section 2, We first introduce the Landau-de Gennes model, and then discuss the boundary conditions after nondimensionalizing the model. In Section 3, we obtain the free-energy minimum and visualize the main numerical results by numerically solving the model. Finally, some concluding remarks are made in Section 4.

2 Model and method

2.1 Landau-de Gennes model

Landau-de Gennes (LdG) model is a widely used model for nematic LCs systems [18], in which the alignment of nematic LCs is described by a symmetric, traceless 3×3 matrix, known as the \mathbf{Q} -tensor order parameter. Here the three eigenvalues of \mathbf{Q} are written as $\lambda_1, \lambda_2, \lambda_3$. \mathbf{Q} is isotropic when $\lambda_1 = \lambda_2 = \lambda_3 = 0$. \mathbf{Q} is uniaxial and can be expressed as $\mathbf{Q} = s(\mathbf{nn} - \frac{1}{3})$ (\mathbf{n} is the director vector) when any two of the eigenvalues equal to each other. Otherwise \mathbf{Q} is biaxial.

In LdG model, the energy functional in the region Ω takes the following form:

$$F[\mathbf{Q}] = \int_{\Omega} f_b(\mathbf{Q}) + f_e(\mathbf{Q}) \, dx. \quad (2.1)$$

Here the bulk energy density is

$$f_b(\mathbf{Q}) = \frac{A}{2} \text{Tr} \mathbf{Q}^2 - \frac{B}{3} \text{Tr} \mathbf{Q}^3 + \frac{C}{4} (\text{Tr} \mathbf{Q}^2)^2, \quad (2.2)$$

and the elastic energy density is

$$f_e(\mathbf{Q}) = \frac{L}{2} \mathbf{Q}_{ij,k} \mathbf{Q}_{ij,k}, \quad (2.3)$$

where A , B and C are the temperature and material dependent parameters, and L is the elastic parameter. Summation over repeated indices is implied and the comma indicates spatial derivative. In this paper, we study the defect patterns in spherical shell (the middle area between two concentric spherical surfaces) $\Omega = \{x \mid R_1 \leq \|x\| \leq R_2\}$. We nondimensionalize the model by defining the characteristic length $\zeta_0 = \sqrt{\frac{27CL}{B^2}}$, reduced temperature $t = \frac{27AC}{B^2}$ and region constants $\tilde{R}_i = \frac{R_i}{\zeta_0}$, and rescaling the variables by $\tilde{x} = \frac{x}{\zeta_0}$, $x \in \Omega$, $\tilde{\mathbf{Q}} = \sqrt{\frac{27C^2}{2B^2}} \mathbf{Q}$, $\tilde{F} = \zeta_0^3 \sqrt{\frac{27C^3}{4B^2L^3}} F$. After dropping all the tildes in $\tilde{F}(\tilde{\mathbf{Q}})$, we obtain

$$F[\mathbf{Q}] = \int_{\Omega} \frac{t}{2} \text{Tr} \mathbf{Q}^2 - \sqrt{6} \text{Tr} \mathbf{Q}^3 + \frac{1}{2} (\text{Tr} \mathbf{Q}^2)^2 + \frac{1}{2} \mathbf{Q}_{ij,k} \mathbf{Q}_{ij,k} \, dx. \quad (2.4)$$

The integration is taken over the rescaled computational domain Ω . After scaling, the eigenvalues of the scaled \mathbf{Q} take values in $(\lambda_{\min}, \lambda_{\max})$, with $\lambda_{\min} = -\frac{1}{3} \sqrt{\frac{27C^2}{2B^2}}$ and $\lambda_{\max} = \frac{2}{3} \sqrt{\frac{27C^2}{2B^2}}$.

The reduced temperature t appears only in the bulk energy term in the LdG model. For $-\infty < t < 1$, the nematic phase is energetically favored by the bulk energy. We use \mathbf{Q}^+ to represent the solution of the global energy minimum of the bulk energy with no boundary constraint, and it is given as follows

$$\mathbf{Q}^+ = s^+ \left(\mathbf{nn} - \frac{\mathbf{I}}{3} \right), \quad (2.5)$$

with

$$s^+ = \sqrt{\frac{3}{2}} \cdot \frac{3 + \sqrt{9 - 8t}}{4}. \quad (2.6)$$

Under certain boundary condition (BC), \mathbf{Q}^+ may no longer be the minimum of the total energy, and defects may arise. Defect patterns are the results of the delicate balance between bulk energy, elastic energy and surface free-energy. The anchoring of molecules on spherical surface can be controlled by adding surface free-energy to the total energy. In the following, we consider two kinds of BCs, namely the radial anchoring condition and the planar anchoring condition.

1. Radial anchoring condition

First we consider the radial anchoring condition, in which the surface free-energy density is given by

$$f_s = \omega (\mathbf{Q}(x) - \mathbf{Q}^+(x))^2, \quad (2.7)$$

where \mathbf{Q}^+ is given in Eq. (2.5) at $x \in \partial\Omega$. ω is the constant which controls the relative strength of BC. The physical meaning of this BC is that all the LC molecules align perpendicular to the sphere surface, with alignment strength equals to s^+ which minimize the bulk energy.

2. Planar anchoring condition

Then we consider the more complex planar anchoring condition

$$\mathbf{Q}x = \lambda_\nu x, \quad (2.8)$$

where x is the normal direction of the surface and $\lambda_{\min} \leq \lambda_\nu < 0$ is a constant. λ_ν measures the strength of compression imposed on the LC molecules at the boundary along the normal direction. When $\lambda_\nu = \lambda_{\min}$, all the molecules aligned in the plane perpendicular to x . We define the surface free-energy density as

$$f_s = \omega \|(\mathbf{Q} - \lambda_\nu \mathbf{I})x\|^2, \quad x \in \partial\Omega, \quad (2.9)$$

where λ_ν can be different values and we assume $\lambda_\nu = -\frac{s^+}{3}$, in which s^+ is given in Eq. (2.6).

A spherical shell is built by two concentric spheres, and they can have different topological constraints for LC molecules. For example, we can take a boundary condition combination which has radial anchoring condition for the inner surface and planar anchoring condition for the outer surface, or vice versa.

2.2 Numerical method

An equilibrium configuration corresponds to an energetically favored state, so our goal is to find $\mathbf{Q}(\mathbf{x})$ that minimize the total free-energy. Here we numerically solve the LdG model with the spectral method based on Zernike polynomial expansion. By using Zernike polynomial to expand \mathbf{Q} -tensor, we treat the expansion coefficients as variables and use BFGS algorithm to minimize the objective function. A function defined in a unit ball can be expanded in terms of Zernike polynomials, and the method is introduced in Ref. [1], so we do not go through the detail here.

In order to expand \mathbf{Q} -tensor by using Zernike polynomials, we change the computational region to the region inside unit ball. For the shell $\Omega = \{\mathbf{x} \mid R_1 \leq \|\mathbf{x}\| \leq R_2\}$, we rescale the variables by $\hat{r} = \frac{r-R_1}{2(R_2-R_1)} + \frac{1}{2}$, $\hat{\theta} = \theta$, $\hat{\phi} = \phi$ ((r, θ, ϕ) are spherical coordinates). This transformation is valid only for the normal spherical shell, which means that $R_1 \neq 0$ and $R_2 \neq \infty$. The corresponding coordinate transformation under the Cartesian coordinate system is

$$\begin{aligned}\hat{x} &= \frac{x}{2(R_2-R_1)} + \frac{R_2-2R_1}{2(R_2-R_1)} \frac{x}{r}, \\ \hat{y} &= \frac{y}{2(R_2-R_1)} + \frac{R_2-2R_1}{2(R_2-R_1)} \frac{y}{r}, \\ \hat{z} &= \frac{z}{2(R_2-R_1)} + \frac{R_2-2R_1}{2(R_2-R_1)} \frac{z}{r}.\end{aligned}\quad (2.10)$$

The rescaled computational domain is $\hat{\Omega} = \{\mathbf{x} \mid \frac{1}{2} \leq \|\mathbf{x}\| \leq 1\}$. The free-energy functional becomes

$$\begin{aligned}F[\mathbf{Q}] &= \int_0^{2\pi} \int_0^\pi \int_{\frac{1}{2}}^1 \left(\frac{t}{2} \text{Tr} \mathbf{Q}^2 - \sqrt{6} \text{Tr} \mathbf{Q}^3 + \frac{1}{2} (\text{Tr} \mathbf{Q}^2)^2 \right. \\ &\quad \left. + \frac{1}{2R^2} \mathbf{Q}_{ij,k} \mathbf{Q}_{ij,k} \right) E(\hat{r}) \sin \hat{\theta} d\hat{r} d\hat{\theta} d\hat{\phi},\end{aligned}\quad (2.11)$$

where $E(\hat{r}) = A\hat{r}^2 + B\hat{r} + C$,

$$\begin{aligned}A &= 8(R_2 - R_1)^3, \\ B &= 8(R_2 - R_1)^2(2R_1 - R_2), \\ C &= 2(R_2 - R_1)(2R_1 - R_2)^2,\end{aligned}\quad (2.12)$$

where $\mathbf{Q}_{ij,k}$ still expresses the partial derivatives of \mathbf{Q} respect to original coordinates x, y, z . Using (q_x, q_y, q_z) express the partial derivatives of components of \mathbf{Q} respect to x, y, z , the partial derivatives can be calculated by the following formula

$$\begin{pmatrix} q_x \\ q_y \\ q_z \end{pmatrix} = \begin{pmatrix} \frac{\partial \hat{x}}{\partial x} & \frac{\partial \hat{y}}{\partial x} & \frac{\partial \hat{z}}{\partial x} \\ \frac{\partial \hat{x}}{\partial y} & \frac{\partial \hat{y}}{\partial y} & \frac{\partial \hat{z}}{\partial y} \\ \frac{\partial \hat{x}}{\partial z} & \frac{\partial \hat{y}}{\partial z} & \frac{\partial \hat{z}}{\partial z} \end{pmatrix} \begin{pmatrix} q_{\hat{x}} \\ q_{\hat{y}} \\ q_{\hat{z}} \end{pmatrix} = J \begin{pmatrix} q_{\hat{x}} \\ q_{\hat{y}} \\ q_{\hat{z}} \end{pmatrix}, \quad (2.13)$$

where J is the transformation matrix.

Because \mathbf{Q} is a traceless symmetrical matrix, so it can be expressed as the following form:

$$\mathbf{Q} = \begin{pmatrix} q_1 & q_2 & q_3 \\ q_2 & q_4 & q_5 \\ q_3 & q_5 & -q_1 - q_4 \end{pmatrix}. \quad (2.14)$$

Here we expand $q_i, i = 1, \dots, 5$ in Zernike polynomials as follow

$$q_i(r, \theta, \phi) = \sum_{m=1-M}^{M-1} \sum_{L=|m|}^{L-1} \sum_{n=l}^{N-1} A_{nlm}^{(i)} Z_{nlm}(r, \theta, \phi), \quad (2.15)$$

where $N \geq L \geq M \geq 0$. The choice of N, L, M need to be adjusted to get the best performance. What we did is to start with some moderate N, L, M and gradually increase some or all of them until the numerical solution converge, i.e., no significant change in the value of free-energy. So given $A_{nlm}^{(i)}$, we can calculate the free-energy and partial derivatives of free-energy function respect to $A_{nlm}^{(i)}$ by numerical integration.

3 Results and discussion

To visualize the tensor field, we use the ellipsoid to express \mathbf{Q} . Here three semi-principle axes of ellipsoid are the three eigenvectors of \mathbf{Q} with lengths equal to the corresponding $\lambda_i + \frac{1}{3}$, in which λ_i represents the eigenvalues of \mathbf{Q} before rescaling. In this representation, an isotropic \mathbf{Q} is shown as a ball and a uniaxial \mathbf{Q} with positive (negative) s is prolate (oblate).

In order to describe the biaxial properties of the \mathbf{Q} -tensor, we define [16]

$$\beta = 1 - 6 \frac{(\text{tr} \mathbf{Q}^3)^2}{(\text{tr} \mathbf{Q}^2)^3}. \quad (3.1)$$

$\beta = 0$ represents that \mathbf{Q} is pure uniaxial while $\beta \neq 0$ corresponds to the biaxial \mathbf{Q} . To visualize the defects, we define [20]

$$c_l = \lambda_1 - \lambda_2, \quad (3.2)$$

where $\lambda_1 \geq \lambda_2 \geq \lambda_3$. At the defect point, $c_l = 0$. Here we use the iso-surface of $c_l = \delta$ to indicate where the defect is, in which δ is a small positive constant.

3.1 Transitions of defect patterns

First we consider planar anchoring condition on both inner and outer surfaces of the shell. In the limit that the thickness of the shell goes to zero, the system becomes a 2D LC-sphere, which has been studied by many other researchers [2, 3, 8, 13]. There are at least

three defect configurations on the spherical surface [2,3], namely the splay, rectangle and tennis-ball. Cheng [2] pointed out that the splay and rectangle configurations are metastable in a 2D tensor model. In our simulation, the splay and rectangle configurations are always unstable when the thickness of the shell is small but is not zero. Moreover, during the optimization process, the local derivatives near these two configurations can be very small but not zero, and these two configurations eventually lose stability and switch to the tennis-ball configuration after a sufficiently long iteration. In this case, a very thin spherical shell is not entirely equivalent to a spherical surface. It is unrealistic to treat molecules on the sphere have zero thickness.

After combining the above inner and outer BCs, the defect structures become 2D defect namely \mathbf{Q} has similar, even equal distribution on arbitrary spherical surface of shell when the shell is thin enough. Fig. 1 illustrates three 2D configurations for the different temperature t and the outer radius R_2 . Fig. 1 (a) is a tennis-ball solution in which four $+1/2$ short disclination lines are inscribed in the shell. The disclination lines start appear from the inner surface and extend to the outer surface, and the lines form a regular tetrahedron on each layer between two surfaces. In the case of thin shell, Fig. 1 (b) and (c) give two other 2D configurations which only exist at high temperature. Fig. 1 (b) shows a 2D oblate solution which is similar to the radial hedgehog solution, in which \mathbf{Q} is uniaxial everywhere and satisfies radial symmetry. The director vector \mathbf{n} align along the direction of radius on each point in Fig. 1 (b), which gives no defect in this configuration. Fig. 1 (c) shows a 2D single-single core solution, which contains two $+1$ disclination lines. This configuration is a compression form of the inner and outer single-core configurations in the shell. This solution is rotationally symmetric around the disclination line and has oblate \mathbf{Q} -tensor along the symmetric axis. In addition, we find that the configuration shown in Fig. 1 (c) disappears and converts to the configuration shown in (b) as the shell becomes thinner.

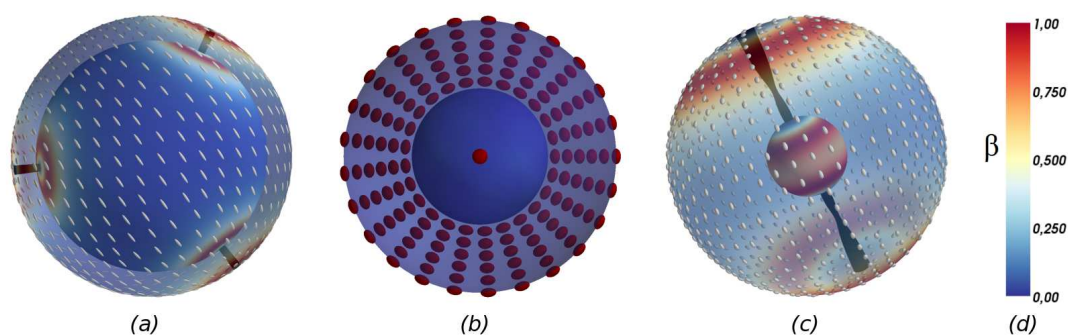


Figure 1: The 2D solutions for the planar anchoring condition on both inner and outer spheres with different t and R_2 (a: $t = -5$, $R_2 = 1.2$; b: $t = 0.8$, $R_2 = 2$; c: $t = 0.8$, $R_2 = 3.34$) and fixed $R_1 = 1$. β is shown in color with red corresponds to biaxial and blue uniaxial. Ellipsoids represent the \mathbf{Q} -tensor. (a): Three-dimensional view of tennis-ball solution; (b): A sliced view of the uniaxial solution; (c): 2D single-single core solution. The black pipes inside the shell are the iso-surface of c_1 with values equal to: (a) $c_1 = 0.04$, (c) $c_1 = 0.002$.

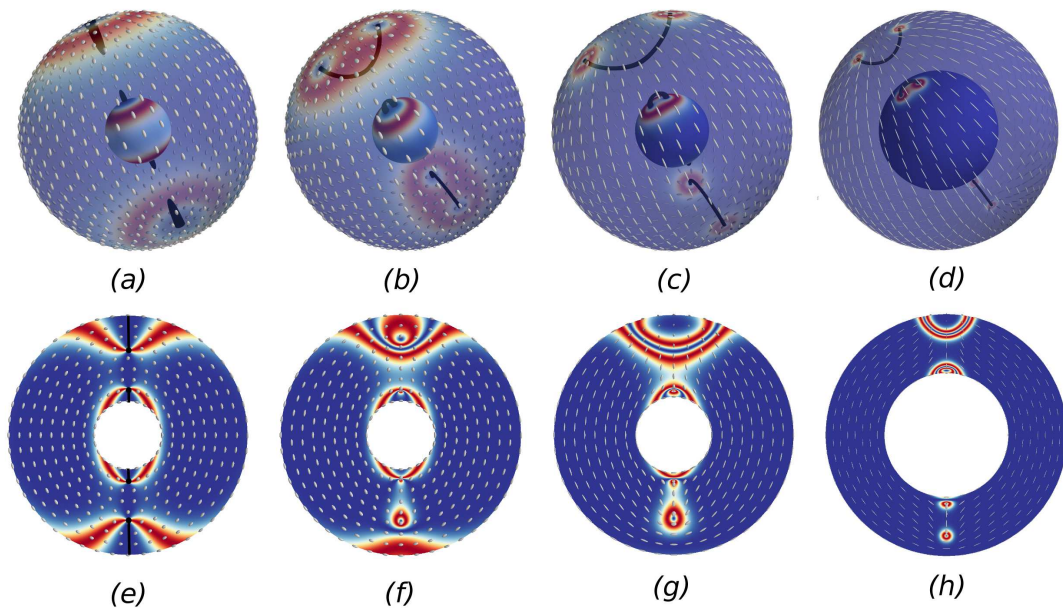


Figure 2: Four stable solutions for the planar anchoring condition on both inner and outer spheres with different t , R_1 and R_2 (a and e: $t=0.5$, $R_1=1$, $R_2=3.5$; b and f: $t=0.1$, $R_1=1$, $R_2=3.5$; c and g: $t=-4$, $R_1=1$, $R_2=3.15$; d and h: $t=-8$, $R_1=4$, $R_2=7.8$). Color corresponds to β , ranging from 0 (blue) to 1 (red). The iso-surfaces of c_l have the values equal to (a): $c_l=0.002$; (b): $c_l=0.012$; (c): $c_l=0.05$; (d): $c_l=0.15$. (a-d) Three-dimensional view. (e-h) Sliced view showing the inside of the LC shell. The cutting plane in (e) pass through the symmetric axis. And the cutting plane in (f-h) is determined by the sphere center and a pair of defect points on the surface. The thick black lines in (e) represent four segments of +1 disclination lines.

As the thickness of the shell increases, many 3D configurations appear as shown in Fig. 2. Fig. 2 (a) shows an rotationally symmetric solution which contains four segments of +1 disclination lines on the two poles of the surfaces. For all these four disclination lines in Fig. 2 (a), an endpoint of each line is isotropic [5] and buried inside the shell, while the another endpoint stays on the sphere. Around each defect point on disclination lines, there is a ring of biaxial region which is indicated by the red color in the figures. The state in Fig. 2 (a) only exists at the high temperature. And as the thickness of the shell increases, the stable solution converts from Fig. 1 (b) to Fig. 1 (c), and then transforms to Fig. 2 (a). Fig. 2 (b-d) show inner double-core plus outer double-core, inner double-core plus outer split-core and inner split-core plus outer split-core configurations respectively. Split-core and double-core are distinguished by the shape of biaxial region on the surface. The two endpoints of disclination line are surrounded by two biaxial ring in split-core, while the two endpoints of disclination line are surrounded by one biaxial ring in double-core. A common feature of these structures shown in Fig. 2 (b-d) is that each structure has four disclination lines in which two are parallel to each other on one side, and two are perpendicular to each other on opposite sides. Fig. 2 (e-h) show β and \mathbf{Q} inside the shells. It is easy to see that all the configurations shown in Fig. 2 are the combinations of

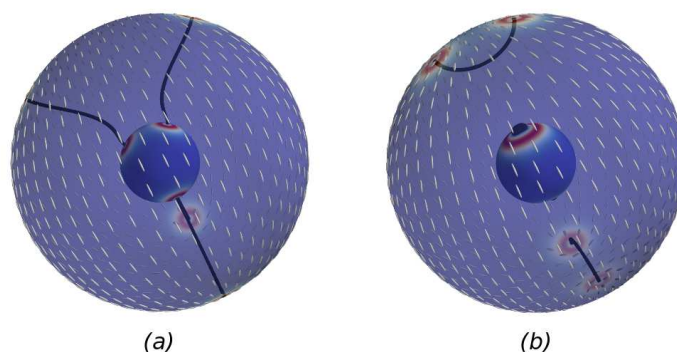


Figure 3: Two stable solutions under $t = -5$, $R_1 = 1$ with planar anchoring condition on both inner and outer spheres. Outer radii R_2 equal to (a: $R_2 = 3.6$; b: $R_2 = 3.61$). The iso-surface of c_1 has the value equals to $c_1 = 0.05$ in (a-b).

single-core, double-core and split-core. In our results, the defect patterns derived by the outer sphere are consistent with the configurations in the spherical droplet [1]. And the defect patterns caused by the inner sphere are consistent with the configurations outside of the solid ball [7, 11].

When the shell is thin, the defect has 2D structures, and when shell is thick, the defect has 3D structures. We aim to study how the 2D structures lose their stability and change to the 3D structures as the thickness of the shell increases, we increase R_2 slowly and inspect how the defect patterns change when R_1 is fixed. We find that the four disclination lines in Fig. 1 (a) will bend into the shapes in Fig. 3 (a) as R_2 increases at the low temperature. Because of this special defect structure, the four defect points on each layer no longer keep a regular tetrahedron shape, but change to a tetrahedron which has four congruent isosceles triangles. We call this kind of configuration the tennis-ball family configuration. Considering the fixed temperature $t = -5$, the configuration change from Fig. 3 (a) to Fig. 3 (b) if $R_2 > R^*$ where $R^* = 3.6$ is the transition point. During this process, the transition of defect patterns from 2D to 3D is discontinuous. At the high temperature, the tennis-ball family structure shown in Fig. 4 (a) changes to the structure shown in Fig. 4 (b) in which a pair of disclination lines touch each other on an intermediate point as R_2 increases. Increasing the thickness, the disclination lines shown in Fig. 4 (b) split into four hemicycle disclination lines, and change to the inner double-core plus outer split-core configuration as given in Fig. 4 (c). Different from the discontinuous transition at the low temperature, the transition of defect patterns from 2D to 3D is continuous at the high temperature.

For illustrating the phase diagram precisely, we call the defect patterns of tennis-ball family shown in Fig. 3 (a) and Fig. 4 (a) 2D configuration, and call the defect pattern shown in Fig. 4 (b) an intermediate state between 2D and 3D configurations. We compute the phase diagram shown in Fig. 5 with R_1 equals to 1, and confirm that there is no transition region when the configuration changes from 2D to 3D under low temperature

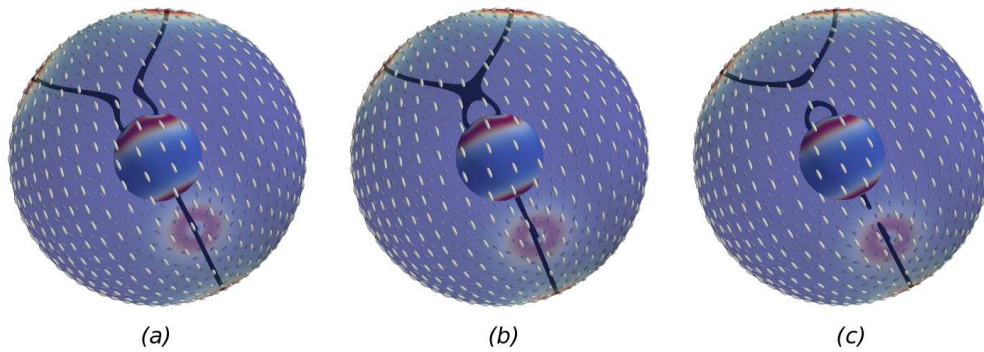


Figure 4: Three stable solutions under $t = -0.4$, $R_1 = 1$ with planar anchoring condition on both inner and outer spheres. Outer radii R_2 equal to (a: $R_2 = 3.25$; b: $R_2 = 3.29$; c: $R_2 = 3.34$). The iso-surface of c_l has the value equals to $c_l = 0.02$ in (a-c).

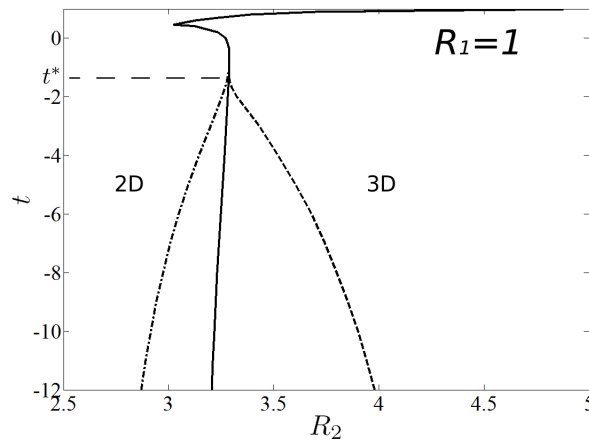


Figure 5: Phase diagram for the planar anchoring condition on both inner and outer spheres.

assumption. The left side of dotted-dashed line keeps only 2D configuration, and the right side of dashed line keeps only 3D configuration in the phase diagram. Both 2D and 3D configurations exist in the region between the dotted-dashed and dashed lines, in which the 2D (3D) configuration has less energy than the 3D (2D) configuration in the region between the dotted-dashed (dashed) line and the solid line. We define the temperature below t^* given in Fig. 5 is low temperature, and the temperature above t^* is high temperature. From the phase diagram, it also approve that the transition between 2D and 3D configurations is discontinuous when $t < t^*$, and it's continuous when $t > t^*$ as we observed in numerical results.

For the spherical shell with radial anchoring conditions on both inner and outer spheres, we obtain the radial-hedgehog solution in which \mathbf{Q} is prolate everywhere in the shell and satisfies the radial symmetry. Majumdar et al. [26] studied the stability of the

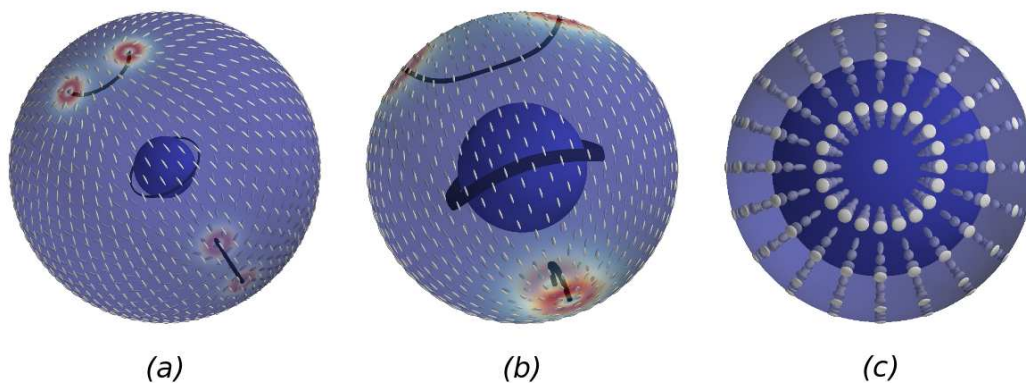


Figure 6: Three stable solutions under $t = -3$, $R_1 = 1$ with radial anchoring condition on the inner surface and planar anchoring condition on the outer surface. Outer radii R_2 equal to (a: $R_2 = 5$; b: $R_2 = 2.4$; c: $R_2 = 1.4$). The iso-surface of c_l has the values equal to: (a) $c_l = 0.05$, (b) $c_l = 0.03$.

radial-hedgehog solution on 3D spherical shell. They proved that the radial-hedgehog solution is the unique global Landau-de Gennes energy minimum for a sufficiently narrow spherical shell, for all temperatures below the nematic supercooling temperature.

We also consider the shell with radial anchoring condition on the inner sphere and planar anchoring condition on the outer sphere. When the thickness of the shell is large enough, the structures we get are the combinations of single-core, double-core, split-core and Saturn-ring. But as the thickness decreases, these structures change also. Considering the fixed temperature $t = -3$, the change process is shown in Fig. 6. Fig. 6 (a) shows a configuration which has one $-1/2$ disclination ring around the inner sphere and two hemicycle disclination lines on the outer sphere. Obviously this structure is a combination of split-core and Saturn-ring. When we decrease the outer sphere radius in Fig. 6 (a) to 2.4, we obtain the solution given in Fig. 6 (b) which has some distortion. Because of the interaction between two kinds of disclination lines, the disclination ring in the shell bends from a circular ring to a saddle shape ring. This shows that the disclination lines feel stronger interaction to each other when the thickness of the shell is small. Continuing to decrease the thickness, we can get a uniaxial solution as shown in Fig. 6 (c). \mathbf{Q} in this configuration is uniaxial everywhere and satisfies the radial symmetry. \mathbf{Q} changes from prolate to oblate and s changes from s^+ to $-s^+/2$ continuously as radius increases. This configuration can be regarded as a 2D configuration because the director vector \mathbf{n} has uniform distribution on every layer of spherical shell.

3.2 Discussion of topological charge

In this subsection we mainly discuss the characterization of defects in 2D and 3D spaces. For the case of 2D space, winding number is an appropriate metric to defects. Winding number can classify all kinds of defects on 2D surface, because only point defects exist.

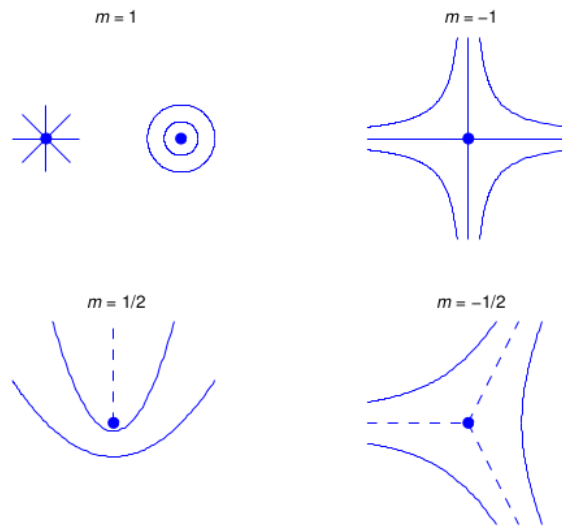


Figure 7: Several kinds of point defects. The solid dots in figures represent the defects, and the tangential direction of solid line represents the eigenvector corresponding to the largest eigenvalue.

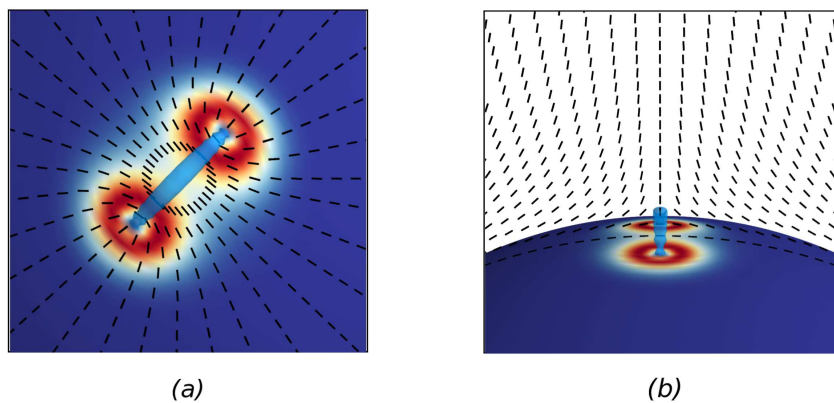


Figure 8: Two side views of split-core configuration near the inner surface of shell. Figure (a) displays the distribution of LC molecules near the defect points on the spherical surface. Figure (b) displays the distribution of LC molecules on the normal plane of the disclination line's midpoint. The black short lines in figures represent the eigenvector corresponding to the largest eigenvalue. The pipes are the iso-surface of $c_l = 0.08$.

Several kinds of point defects are shown in Fig. 7. For the case of 3D space, there are two kinds of measures to characterize the defects, respectively winding number and topological charge. We know that the disclination lines in 3D space can be classified according to their homotopy [4], in which topological charge has two categories: 0 or 1/2. However, winding number and topological charge are incompatible for some disclination lines, which can be illustrated by the disclination line shown in Fig. 8. Fig. 8 shows two side

views of split-core on the inner surface of the shell. The black short lines in figures represent the eigenvector corresponding to the largest eigenvalue, which can be regarded as the local director. The disclination line surrounded by the blue pipe in Fig. 8 is in the $1/2$ topological charge category. But the winding numbers on this disclination line are not equal, for instance, the winding numbers of the two endpoints on the surface are $+1/2$, and the winding numbers of the midpoint shown in Fig. 8 (b) is $-1/2$. So winding number as an intuitive concept does not match the topological charge in 3D space, which means that the winding number is not good at describing the global properties of disclination lines. Meanwhile, the simple classification determined by topological charge can not depict the variety winding numbers of disclination lines clearly. This leads us to think how to effectively define a quantity in 3D space to crisply distinguish various kinds of disclination lines.

4 Conclusion

In this paper, we investigate defect patterns in three-dimensional spherical shell with LdG model. By using the spectral method, we can calculate many interesting configurations under different parameters. Based on the observations made from these results, we are ready to summarize some general rules. First we try to understand the relationship between 2D spherical surface and 3D spherical shell, and we find that the structures exist on the spherical surface might not exist in the thin spherical shell, such as splay and rectangle structures. It means that some configurations only occur when the thickness of LC molecules layer equals to zero, which is unrealistic. So it is not entirely feasible to process a thin spherical shell as a spherical surface. Then we study the transition between 2D configurations and 3D configurations in spherical shell. When the thickness of shell is large enough, the defect patterns are 3D configurations, which are the combinations of defect patterns derived by two boundary surfaces. But when the thickness of shell is thin enough, 2D configurations are energetically favored because of the lack of radial space. For the shell with planar boundary condition on both inner and outer surfaces, the transition between 2D configurations and 3D configurations might be continuous or discontinuous, depending on the temperature.

Acknowledgments

Dr. Yucheng Hu provides many useful suggestions. P. Zhang is partly supported by National Natural Science Foundation of China (Grant No. 11421101 and No. 11421110001).

References

- [1] Y. C. Hu, Y. Qu and P. W. Zhang, On the disclination lines of nematic liquid crystals, Commun. Comput. Phys., 19 (2016), 354-379.

- [2] H. Cheng and P. W. Zhang, A tensor model for liquid crystals on a spherical surface, *Sci. China Math.*, 56 (2013), 2549-2559.
- [3] W.-Y. Zhang, Y. Jiang and J. Z. Y. Chen, Onsager model for the structure of rigid rods confined on a spherical surface, *Phys. Rev. Lett.*, 108 (2012), 057801.
- [4] O. D. Lavrentovich, *Defects in Liquid Crystals: Surface and Interfacial Anchoring Effects, in Patterns of Symmetry Breaking*, Springer Netherlands, Dordrecht, 2003, 161-195.
- [5] S. Kralj, R. Rosso and E. G. Virga, Fingered core structure of nematic boojums, *Phys. Rev. E*, 78 (2008), 031701.
- [6] T. C. Lubensky, David Pettey, Nathan Currier and Holger Stark, Topological defects and interactions in nematic emulsions, *Phys. Rev. E*, 57 (1998), 610.
- [7] M. Tasinkevych, N. Silvestre and M. M. Telo da Gama, Liquid crystal boojum-colloids, *New J. Phys.*, 14 (2012), 073030.
- [8] D. R. Nelson, Toward a tetravalent chemistry of colloids, *Nano Lett.*, 2 (2002), 1125-1129.
- [9] T. Lopez-Leon, V. Koning, V. Vitelli, K. B. S. Davaiah and A. Fernandez-Nieves, Frustrated nematic order in spherical geometries, *Nature Physics*, 7 (2011), 391.
- [10] V. Vitelli and D. R. Nelson, Nematic textures in spherical shells, *Phys. Rev. E*, 74 (2006), 021711.
- [11] M. Ravnik and S. Zumer, Landau-de Gennes modelling of nematic liquid crystal colloids, *Liq. Cryst.*, 36 (2009), 1201.
- [12] P. Poulin and D. A. Weitz, Inverted and multiple nematic emulsions, *Phys. Rev. E*, 57 (1998), 626.
- [13] S. Kralj, R. Rosso and E. G. Virga, Curvature control of valence on nematic shells, *Soft Matter*, 7 (2011), 670-683.
- [14] M. A. Bates, G. Skačej and C. Zannoni, Defects and ordering in nematic coatings on uniaxial and biaxial colloids, *Soft Matter*, 6 (2010), 655-663.
- [15] A. Majumdar, Equilibrium order parameters of nematic liquid crystals in the Landau-de Gennes theory, *Eur. J. Appl. Math.*, 21 (2010), 181-203.
- [16] S. Mkaddem and E. Gartland Jr, Fine structure of defects in radial nematic droplets, *Phys. Rev. E*, 62 (2000), 6694.
- [17] T. Porenta, M. Ravnik and S. Zumer, Effect of flexoelectricity and order electricity on defect cores in nematic droplets, *Soft Matter*, 7 (2011), 132.
- [18] P. G. de Gennes and J. Prost, *The physics of liquid crystals*, Oxford University Press, Oxford, second ed., 1995.
- [19] F. H. Lin and C. Liu, Static and dynamic theories of liquid crystals, *J. Partial Differ. Equ.*, 14 (2001), 289-330.
- [20] A. C. Callan-Jones, R. A. Pelcovits, V. A. Slavin, S. Zhang, D. H. Laidlaw and G. B. Loriot, Simulation and visualization of topological defects in nematic liquid crystals, *Phys. Rev. E*, 74 (2006), 061701.
- [21] D. S. Miller, X. Wang and N. L. Abbott, Design of functional materials based on liquid crystalline droplets, *Chem. Mater.*, 26 (2013), 496-506.
- [22] S. Kralj, E. G. Virga and S. Žumer, Biaxial torus around nematic point defects, *Phys. Rev. E*, 60 (1999), 1858-1866.
- [23] F. Zernike, Diffraction theory of the cut procedure and its improved form, the phase contrast method, *Physica*, 1 (1934), 689-704.
- [24] M. Avriel, *Nonlinear programming: analysis and methods*, Courier Dover Publications, 2003.
- [25] T. Lopez-Leon and A. Fernandez-Nieves, Drops and shells of liquid crystal, *Colloid Polym*

- Sci., 289 (2011), 345-359.
- [26] G. Canevari, M. Ramaswamy and A. Majumdar, Radial symmetry on three-dimensional shells in the Landau-de Gennes theory, *Physica D: Nonlinear Phenomena*, 314 (2016), 18-34.
 - [27] S. R. Seyednejad, M. R. Mozaffari and M. R. Ejtehadi, Confined nematic liquid crystal between two spherical boundaries with planar anchoring, *Phys. Rev. E*, 88 (2013), 012508.
 - [28] T. Lopez-Leon, M. A. Bates and A. Fernandez-Nieves, Defect coalescence in spherical nematic shells, *Phys. Rev. E.*, 86 (2012), 030702.
 - [29] David Seč, T. Lopez-Leon, M. Nobili, C. Blanc, A. Fernandez-Nieves, M. Ravnik and S. Žumer, Defect trajectories in nematic shells: Role of elastic anisotropy and thickness heterogeneity, *Phys. Rev. E.*, 86 (2012), 020705.
 - [30] A. Fernández-Nieves, V. Vitelli, A. S. Utada, D. R. Link and M. Márquez, D. R. Nelson and D. A. Weitz, Novel Defect Structures in Nematic Liquid Crystal Shells, *Phys. Rev. Lett.*, 99 (2007), 157801.